# Semi-automatic Segmentation of Prostate by Directional Search for Edge Boundaries

Juha M. Kortelainen, Kari Antila
VTT Technical Research Centre of Finland,
Tampere, Finland
{juha.m.kortelainen, kari.antila}@vtt.fi

Alain Schmitt
Sunnybrook Research Institute,
Toronto, Canada

Charles Mougenot †, Gösta Ehnholm ‡
Philips Healthcare,
†Toronto, Canada
‡Vantaa, Finland

Rajiv Chopra, PhD
University of Texas Southwestern Medical Center,
Dallas, United States

## ABSTRACT

Semi-automatic segmentation of the prostate boundary is presented for the pre-operational images of the MRI-guided ultrasonic thermal therapy of the prostate cancer. The specific deformable surface method is based on firstly fitting an ellipsoid on the given manual landmark points, then modifying the shape of the initialization surface mesh by masking out the regions of the separately segmented bladder and rectum, and finally adapting the surface mesh by searching image for the edge boundaries in the direction of the surface normal. The suggested segmentation method combines information from two types of pre-operational MR-images showing different contrast for the tissue structure. Dice similarity coefficient (DSC) between the semi-automatic segmentation and the manual reference was on average 0.89 for a group of N=5 patients having the MRI guided ultrasound thermal treatment. The robustness of the surface fitting method was tested by simulating 30 randomized initialization sets of the landmark points for each patient, and the resulting standard deviation of DSC was 0.01.

## Keywords

Deformable Surface, Prostate, MRI segmentation.

## 1. INTRODUCTION

Recent studies have shown promising results on applying the MRI guided high-intensity ultrasound for the non-invasive treatment of the localized prostate cancer, using an ultrasound applicator inserted into the urethra to generate thermal coagulation within the target region in the prostate gland [Cho12a]. The prostate boundary identification from the MR-images taken after placement of the ultrasonic transducer is needed to provide exact planning for the applied power and the rotational speed of the multi-element transducer. The segmented prostate boundary might then be used additionally during the ultrasound treatment also, e.g. in visualization of the MRI-thermometry measured on-line temperature map, or in the post-analysis, to estimate treatment outcome together with the separately measured non-perfused volume of the prostate gland.



Both T1- and T2-weighted MR-images are taken during the pre-operational stage of the transurethral ultrasonic treatment of the prostate cancer. They give different contrast between tissue types, and in general, the T1-weighted MRI measures the spin-lattice relaxation time in the longitudinal direction of the main magnetization field after giving the transversal excitation RF-pulse, while the T2-weighted MRI is measuring the spin-spin relaxation time in the transversal direction using different variants of the RF-pulse sequences.

### Related work

The previous studies on the prostate segmentation are in the most cases using statistical parameters trained with a large set of diagnostic T2-weighted MR-images. The anatomical volume and shape of prostate varies strongly, as well as the MR scanners and image acquisition protocols, affecting the image resolution, quality and artefacts. For example, the

 ISBN 978-80-86943-71-8

Miccai 2012 conference challenge on the prostate MR image segmentation (PROMISE12) provided a training data set including 50 MR volume images, collected from four different medical centers, and the best scores were given by an active appearance model (AAM) approach [Mic12a].

Unfortunately, limited number of cases of the transurethral ultrasonic therapy prevents using AAM, and the segmentation of the prostate boundary from the related pre-operational MR images seems to be even more challenging than on the diagnostic MR images. The transurethral ultrasonic applicator causes deformation of the flexible prostate gland, partly intentionally, to bring the transducer into the optimal position inside the prostate for delivering the ultrasonic radiation for the treatment region [NDj12a]. The pre-operational MR-images are taken in strict time limits and may thus have reduced resolution and less quality in comparison with the diagnostic images. The ultrasonic device includes metal parts and can cause also imaging artefacts. Currently, we can only speculate that it might still take several years until this specific treatment method shall be in the clinical use, to provide sufficient amount of training data e.g. for the AAM method.

Therefore, our approach is a semi-automatic segmentation method, using manual landmarks on the prostate boundary. It is also constrained in topology by masking out the regions of the limiting organs, such as bladder and rectum. With this prior information, a surface model is fitted and triangulated for a surface mesh, and then finally adapted by moving the mesh nodes towards the image edges, searched iteratively in the direction of the deformed surface normal.

## 2. STUDY DESCRIPTION

### Measurement protocol

MR images for altogether five subjects, having the MRI guided ultrasound thermal therapy for the prostate cancer, were used in this study for the prostate segmentation. The patients are numbered as P1, P2, P4, P5 and P6, because data for the third patient enrolled was not available. The data was collected during years 2012 and 2013 at the Sunnybrook Health Sciences Centre, Toronto, using 3.0-T Philips Achieva MR-unit. The subjects had given their voluntary acceptance for the study, and they were selected as being scheduled for the radical prostatectomy of the prostate cancer after the ultrasonic therapy.

The prostate treatment and the MR-imaging followed the protocol described in the reference [Cho12a]. Firstly, a T1-weighted *preparation image* was taken to localize the position of the manually inserted transurethral ultrasonic transducer. After the transducer was re-positioned into the correct location using an intermediate MR imaging, a T2-weighted *planning image* was taken to provide the final operation parameters for the ultrasonic transducer. During the ultrasonic treatment, sequences of 2D MR-images, using the proton resonance frequency shift thermometry, were scanned continuously to have the on-line temperature maps of the ultrasound operation in the orthogonal plane with the transducer elements. After the treatment, two T1-weighted 3D MR-images were taken before and after administration of the contrast agent to show the non-perfused volume of the coagulated matter.

The prostate segmentation presented in this paper is targeted for the T2-weighted *planning image*, but also the T1-weighted *preparation image* is used to provide additional information about the prostate boundary. The images have different MR scanning parameters for the origin, field of view and resolution, but they are resampled afterwards for the prostate segmentation. The resampled isotropic images have the resolution of 0.5 mm and volume sizes of 519x519x198 (ap, rl, fh). The reference manual segmentation of the prostate boundary from the *planning image* was done by an expert using a preliminary software version for the 3D visualization, and is shown with the red contour in the figures of this paper.

### Contrast of prostate boundary

A major problem on the segmentation of the prostate from the T2-weighted planning image is the large variation in the MRI signal intensity of the prostate in comparison with the surrounding tissue. Figure 1 shows the planning image for the subject P1 for the orthogonally oriented slices, which are selected from the center location of the ultrasonic transducer. The dashed lines show the crossing position of the selected slices, and the coronal plane is placed orthogonally with the straight lined transducer element. The ultrasonic transducer inside the urethra is found as a low intensity, about 5 mm thick region, in parallel with the dashed crossing lines (a dot in the first coronal slice, the horizontal line in the transverse slice and the vertical line in the sagittal slice).

The manually segmented prostate boundary is shown with a red colored contour line in each orientation. For this example graph, the 12 landmarks needed for the initialization of the semi-automatic segmentation, are selected by placing four landmarks on each orthogonal central slice, distributed with equal 90 degrees angles from the slice crossing point as an origin.

Figure 1 shows that the grayscale difference of the planning image across the prostate boundary may have an opposite direction in the different regions. For example, the image intensity is decreasing for the inwards direction of the prostate at the upper

(anterior) side of both the coronal and transverse oriented slices, while at some surface regions at the bottom (posterior) side of the graphs the intensity is increasing. This variation in the contrast of the prostate boundary in the T2-weighted MRI is caused firstly by different structure of the surrounding tissue, and secondly on the imaging artefacts, which can be caused i.e. by the ultrasonic transducer device in the urethra.

Figure 2 shows the T1-weighted preparation image of the subject P1 with the same manual segmentation contour and landmarks as in Figure 1. On the upper side of the graphs the intensity gradient across the prostate boundary is increasing, while for some other regions there seem to be no significant contrast across the prostate boundary. Figure 3 shows a similar comparison for the patient P6 but for two slice orientations only. In this case, the prostate boundary is again visible for the planning image in the top graphs, although the grayscale intensity behaves somewhat differently over the prostate gland in comparison with Figure 1. The bottom graph preparation images of Figure 3 do not show good contrast on the prostate boundary. Also, the boundary between the prostate and bladder is not well aligned between the preparation and planning images, shown with arrows.

In conclusion, the T2-weighted planning image shows a good contrast all over the prostate boundary, but with a variable gradient vector direction, while the T1-weighted preparation image shows the prostate consistently with a similar or higher grayscale intensity than the surrounding tissue, but the prostate can be misaligned, or the boundary contrast is not sufficient in some regions.

## Segmentation evaluation methods

For the results section in this paper, the quality of the suggested semi-automatic segmentation of the prostate boundary was measured using the dice similarity coefficient (DSC), which shows the spatial overlap between the segmented and the reference prostate volumes. DSC varies between 0, where no spatial overlap exists, to 1, with a complete overlap [Dic45a, Zou04a].

To evaluate some basic statistics, we simulated 30 different initialization sets of the landmarks for each patient. Each landmark set included 12 points placed randomly over the manually segmented reference surface for the prostate boundary. However, the variation in the location of the landmarks was restricted by the following means. Firstly, the landmarks were divided into three groups, including four landmarks placed on each pre-defined plane in the coronal, transverse and sagittal orientation. Figure 1 shows an example of the placement of the landmarks into three orthogonal slices. The origin of

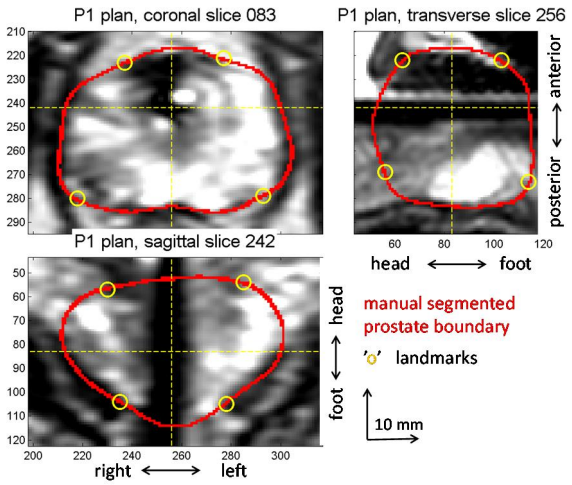


**Figure 1. T2-weighted planning image for patient P1. Red contour shows manual segmentation and yellow 'o' label the landmarks.**

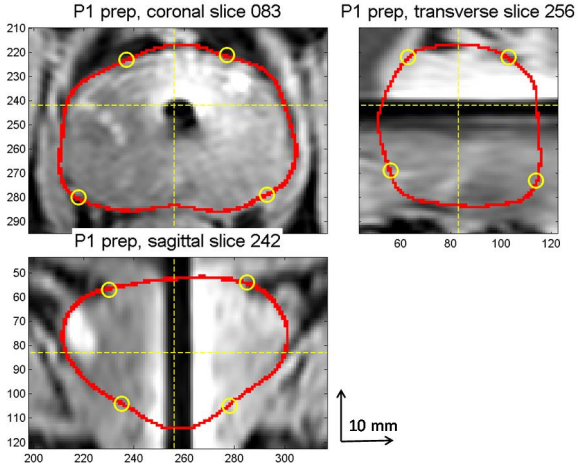


**Figure 2. T1-weighted preparation image for P1. The manual segmentation and landmarks are defined for the planning image in Figure 1.**

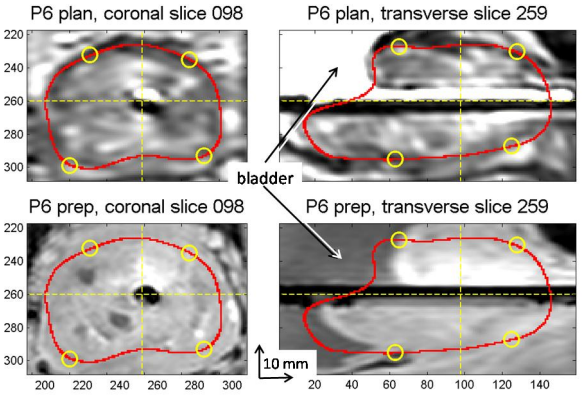


**Figure 3. T2-weighted planning image for P6 in top graphs and T1-weighted preparation image in bottom graphs. Bladder is marked with arrows and prostate boundary against bladder has moved in between images in top and bottom graphs.**

 ISBN 978-80-86943-71-8

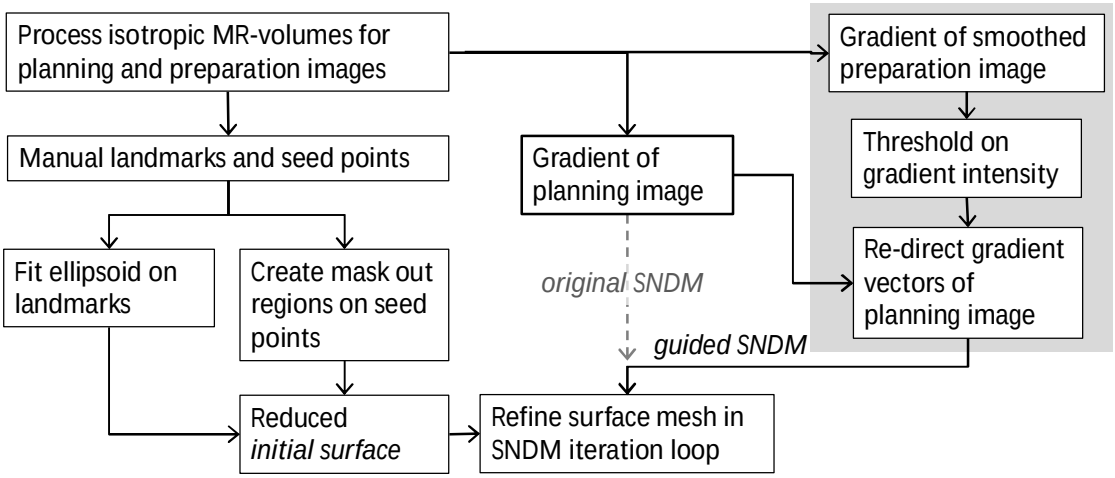


**Figure 4. Graph of segmentation pipeline. Left hand side shows generation of *initial surface*. Testing of *original SNDM* method using only one MR volume image is shown with dashed arrow, and suggested *guided SNDM* method using also additional MR volume image for re-directing gradient vector field is shown in right hand side with grey background.**

slices was set a priori for each patient directly at the center position of the ultrasonic transducer. Based on the origin, each landmark was selected by choosing a point on the reference prostate contour for a set of direction angles. These four angle values are at {-3/4, -1/4, 1/4, 3/4}*π radians in Figure 1.

In the randomized simulation, both the slice origin position and the direction angles were varied. The slice origin was altered in each orthogonal direction from the default origin position using uniformly distributed random variable in the range of ±10 voxels, which corresponds with ±5 mm range for the resampled isotropic images. The position of the slice origin is randomized with such narrow bounds, because in the final application the origin will be set by the middle position of the US-transducer array, which naturally is adjusted carefully into the target position. The four direction angles were varied separately for each orthogonal slice using also uniformly distributed random variable, but by taking care that the distance in between the randomized direction angle values was at least π/8 radians.

We suggest that by this way we can estimate the robustness of the segmentation method on variable position of the landmarks. The segmentation results were compared by calculating the dice similarity with the reference manual segmentation, and finally showing both the averages and standard deviation values for each patient, over the N=30 simulation runs with different landmarks.

## 3. SEGMENTATION ALGORITHM

The suggested prostate segmentation method is based on having an accurate initialization surface. The landmarks are placed on the prostate surface boundary, to create firstly an ellipsoid surface. Additional seed points are needed for both bladder and rectum, one for each, to generate anatomical mask regions to clamp the ellipsoid into a reduced *initial surface*. Finally, the surface mesh is deformed in a controlled way towards potential boundaries in the image, using similar kind of the energy minimization with edge functional as defined for the snakes [Kas88a].

The specific deformable surface method applied in here has been developed originally for the segmentation of the uterine fibroid from T1-weighted post-treatment images of the MRI-guided ultrasonic therapy of the fibroid [Ant14a]. The method is renamed as *Surface Normal Deformable Model* (SNDM) to be more specific. The algorithm seeks for the edges in the direction of the surface normal vector, with the additional constraint for having an increasing intensity for the inwards direction of the initial surface. As the surface bends during iteration, the searching direction for each mesh node varies correspondingly.

As discussed already for Figure 1, the assumption about the increased intensity for the segmented object is not correct for the prostate images. Therefore, our hypothesis is, that the surface can be adapted into the prostate boundary by using the edges in the T2-weighted planning image, which gives sufficient contrast across the prostate boundary, but the accuracy can be improved by using also the T1-weighted preparation image as guiding information for the searching direction in the applicable regions.

Figure 4 shows the segmentation pipeline including the intermediate *initial surface*, and two alternative segmentation results *original* and *guided SNDM*,

which shall all be evaluated in the results section of this paper.

## Initial surface

The initial surface is firstly generated by fitting an ellipsoid for the landmark points with the least squares method [LiQ04a]. The ellipsoid surface is discretized with a triangular mesh, and then further modified to avoid entering into the masked out regions of the bladder and rectum. The latter deforming operation for the initial surface mesh was found to be essential especially on the posterior side boundary of the prostate gland against the rectum, which could not be sufficiently modelled by an ellipsoid.

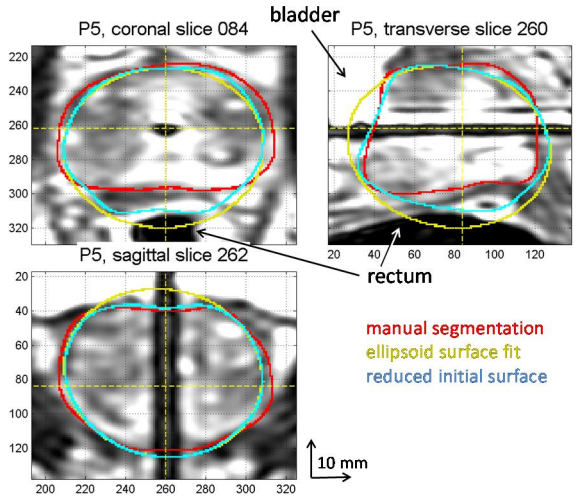


**Figure 5. Manual segmentation, ellipsoid fit and reduced initial surface for patient P5. Bladder and rectum are pointed with arrows.**

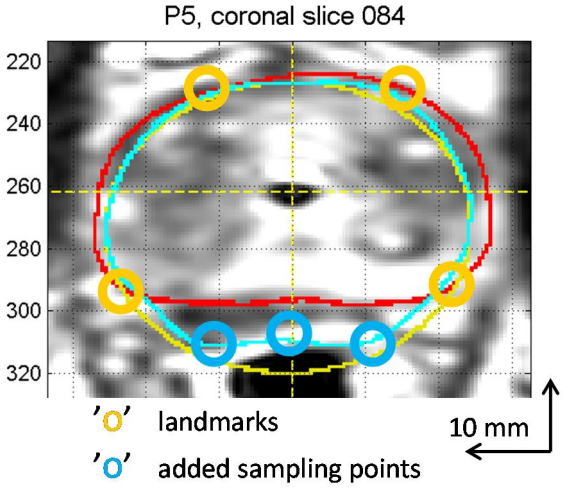


**Figure 6. Patient 5 coronal slice from Figure 5 and additional sampling points (blue 'o'), which are placed in between landmarks (yellow 'o').**

The anatomical mask regions were defined separately for both the bladder and rectum, by firstly giving a manual seed point for each. These both organs have a good contrast on the images, and the mask regions could be segmented with the `RegionGrowing()` function from the Matlab™. The incorrect regions were cleaned out with the morphological operations like the opening to remove thin connections and the filling of holes, and finally the main body of the segmented volume was selected based on the position and volume size. It might be possible to fully automatize this part of the segmentation, because the position of the ultrasonic transducer inside the urethra is a priori known, and so forth the expected positions for both the bladder and rectum could be used for the initialization of the segmentation.

Figure 5 shows an example for the generation of the initial surface. The ellipsoid, fitted on the 12 landmarks, is shown with the yellow color, and it follows the red colored manual segmented prostate sufficiently well. However, the ellipsoid model surface differs more on the boundaries against the bladder and rectum. The bladder is the bright high intensity region in the top left corner of the transverse slice in Figure 5. The rectum is the dark low-intensity region in the bottom side of both the coronal and transverse slices. When testing the direct use of the ellipsoid as an initial surface for the following SNDM algorithm, we ended up to high uncertainty on the final segmentation accuracy, because the ellipsoid follows poorly the corners of the actual prostate boundary. The reduced initial surface, with the light blue colored contour, is clamped in between the masked out regions, and gives an improved shape for the initialization model.

The algorithm to modify the ellipsoid surface mesh for the reduced initial surface follows a free-form deformation (FFD) method, and has been originally developed to register an anatomical surface model, including lungs, myocardium and heart ventricles, into a MRI volume image of the human upper torso [Löt99a]. The algorithm uses a multi-resolution pyramid of the MRI volume image to improve both processing efficiency and robustness. The FFD method was further developed by [Koi04a], to enable using discrete sampling points instead of the anatomical surface model. We applied this by using automatically sampled additional points, to prevent the initial surface to enter into the masked out regions. We firstly calculated intersection between the ellipsoid and the mask region, selected pairs of the landmarks having the intersection surface in between, and finally added three equidistant sampling points on the intersection surface in between each pair of landmarks.

Figure 6 shows an enlarged view for the coronal slice of Figure 5. The masked out region of the rectum is

 ISBN 978-80-86943-71-8

the dark low intensity region in the bottom of the graph, and the initialization ellipsoid is with the yellow colored contour. Three additional points, shown with the blue 'o' marks, are automatically sampled on the intersection surface contour of the rectum and ellipsoid, placed in between the corresponding pair of landmarks shown with the yellow 'o' marks. The reduced initial surface is shown with the bright blue colored contour, and as it approaches the red colored prostate boundary, it gives an improved initialization model for the final SNDM algorithm.

## SNDM iteration loop

The edge tracking external energy functional of the SNDM algorithm uses the gradient of a volumetric image *I*. The gradient is calculated with the 3D Sobel operator. The search is constrained with a directional term D to track only for the edges which have the gradient flow in the expected direction of the initial surface normal vector:

$$E_{edge} = -\|\nabla I\|^2 \cdot D \qquad (1)$$

Term D is calculated as a dot product between the initial surface normal vector and the normalized gradient vector.

The processing is discretized by using the triangulated surface mesh structure. The surface normal vectors (NV) are calculated for each mesh node. The correct *inwards-handedness* of the NV is defined already when the initial surface mesh triangulation is constructed from the fitted ellipsoid. Then, the profile vectors with a limited length are defined for each node in parallel with the NV, extended both for inwards and outwards of the surface. Based on equation (1), the local energy minima are searched over the voxels defined by each profile vector, and the largest consistent deforming region over all the mesh nodes is selected to be modified. The shape of both the selected surface region and the neighborhood is finally regularized by a spatial smoothing, to apply the needed internal energy functional for the method. The goodness-of-fit is determined as the sum of the gradient intensities for the voxels in each mesh node locations, and the fitting process is run iteratively until convergence, or if the maximum number of the iterations is reached. [Ant14a]

The *original SNDM* segmentation method was evaluated also for the results in this paper, by using directly the gradient volume of the T2-weighted planning image as an input for the iteration loop, which is shown with a dashed arrow in Figure 4.

For the suggested *guided SNDM* method, shown with the grey background in the pipeline graph, the T1-weighted preparation image is used to improve the prostate segmentation in the following way: 1) preparation image is smoothed with a Hanning window of the size (15x15x15) voxels, and gradient of the smoothed image is calculated with the Sobel operator, 2) the regions with sufficient gradient intensity are selected by a constant threshold value, 3) in the applicable regions, the planning image gradient vectors are re-oriented for the direction of the preparation image gradients, to be used in the SNDM iteration loop. By this way, the good contrast of the T2-weighted planning image is preserved, but where applicable, the T1-weighted preparation image is guiding the searching direction of the SNDM algorithm. The smoothing of the preparation image is needed firstly to prevent adaptation on the smallest details, and secondly to allow some misalignment between the preparation and planning images.

The constant threshold level of 15, for the gradient intensity of the smoothed T1-weighted preparation image in the *guided SNDM* method, was selected heuristically in purpose to mask out image regions in which the poor signal to noise ratio would lead to unreliable searching direction. The percentage of the selected image region over all five subjects varied in the range of 31.1 % … 37.2 %, with the average value of 34.5 %. The units of both the gradient intensity and the threshold value are corresponding with the original T1-weighted preparation image, having integer values in the range of 0 … 4095.

# 4. RESULTS

The segmentation quality is measured with dice similarity coefficient (DSC) between the calculated and manually segmented prostate boundary. The comparison is given for three different surfaces:

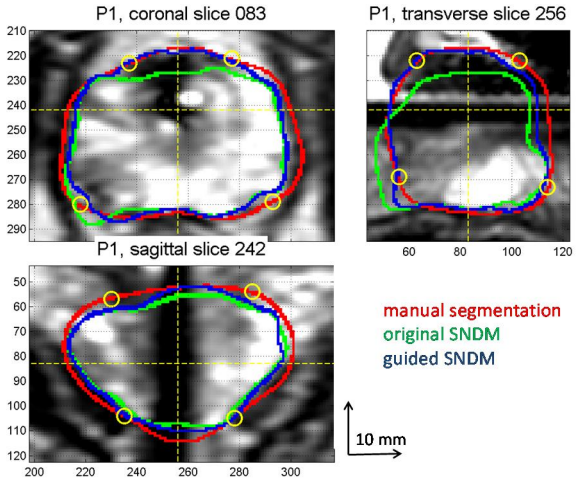


**Figure 7. T2-weighted image for patient 1 with prostate segmentations in comparison. Green contour shows original SNDM fitting for prostate boundary, based on T2-weighted planning image only, and blue contour shows suggested guided SNDM fitting method using T1-weighted preparation image also.**

 ISBN 978-80-86943-71-8

| Pat-ient | model surface | | original SNDM | | guided SNDM | |
|---|---|---|---|---|---|---|
| | mean | std | mean | std | mean | std |
| **P01** | 0.85 | 0.03 | 0.80 | 0.03 | 0.90 | 0.01 |
| **P02** | 0.83 | 0.03 | 0.74 | 0.03 | 0.87 | 0.01 |
| **P04** | 0.84 | 0.04 | 0.71 | 0.04 | 0.89 | 0.01 |
| **P05** | 0.88 | 0.02 | 0.77 | 0.02 | 0.91 | 0.01 |
| **P06** | 0.87 | 0.02 | 0.78 | 0.03 | 0.89 | 0.01 |
| **tot** | **0.85** | **0.03** | **0.76** | **0.03** | **0.89** | **0.01** |

**Table 1. Dice similarity coefficient with randomized landmark positions over N=30 simulations for each patient**

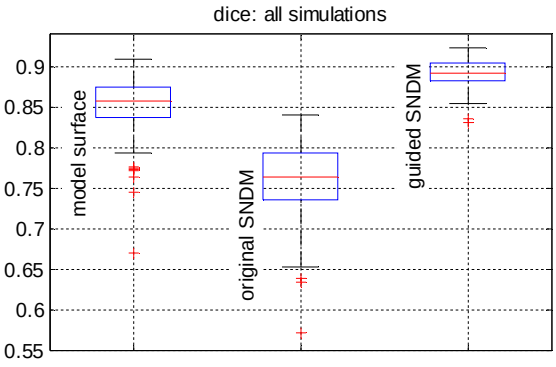


**Figure 8. Boxplot graph showing dice similarity coefficient over all N=5 patients and N=30 randomized landmark simulations. Median value is the red middle line inside the box, and first and third quartiles set bottom and top of the box, correspondingly. Red dots show the outliers.**

firstly for the *initial surface*, secondly for the *original SNDM* method from [Ant14a], using the planning image gradient only, and finally for the suggested *guided SNDM* method, by firstly re-orienting the planning image gradient direction with the gradient of the smoothed preparation image. Figure 7 shows the segmentation results for the patient 1 data. The manual segmentation is shown with the red colored contour and the landmarks are placed in this example figure for their default positions. The original method is shown with the green contour and the suggested guided SNDM method is shown with the blue colored contour.

Table 1 shows both the average DSC and the standard deviations over 30 simulations of the randomized landmark positions for each patient data. The initial surface gave already quite good dice similarity result, having the average of 0.85, but sufficiently high variance. Weakest results gave the original SNDM method, assuming incorrectly always an increasing gradient for the planning image across the prostate boundary. For the case P04 the original method gave the worst average result and also resulted into the largest variance over the simulations. The best result, in both terms of the average DSC and the smallest variance over the landmark simulation, was given by the suggested guided SNDM method.

Figure 8 shows the boxplot graph over the patient data and with the simulated landmark positions. The box middle line shows the median value, and the box range is the lower and upper quartile of data (Q1 and Q3). The whiskers extension from the box is defined as 1.5 times the interquartile range between the Q1 and Q3, unless the maximum or minimum of data values is reached. The outliers exceeding the whiskers are shown with the red dots. The initial surface fits already quite well with the reference prostate boundary based on the median DSC value of 0.86, but the original SNDM segmentation method fails and decreases the DSC value. The suggested guided SNDM segmentation improves the median DSC, and also shows smallest variation over the randomized landmark simulation. The range of the outliers is large already for the initial surface, but with the guided SNDM method the outliers are improved to be almost within the whiskers range.

## 5. DISCUSSION

Most of the referenced prostate segmentation methods could not be applied in here, being based on the statistical shape or appearance parameters which would need a large training data set [Lit14a]. The specific Surface Normal Deformable Model (SNDM) is developed here to restrict the searching space by using both a priori information and sufficiently accurate initialization surface model. The SNDM uses a discrete polygonal mesh as the surface structure, while the original snakes and related volumetric surface methods use spline functions. Other studies using the polygonal meshes allow usually a more generic adaptation, and may have to refine the mesh structure by adding or removing the nodes during the iteration, which is not necessary in the SNDM method. The constrained search in the direction of the surface normal makes the SNDM method even more rigid. Directional search has been applied also in the scope of the Gradient Vector Flow (GVF), which leads to a generic method, but with increased computational complexity due to GVF calculation. [Mon11a]

The semi-automatic algorithms are often selected in the segmentation of the medical images for the practical reasons. The user input for the initialization of the segmentation normally leads to a reliable result, and thus might reduce the manual work needed in the validation of the segmentation result. Also, if the semi-automatic segmentation result is found not valid in a certain region, it can be improved interactively by adding landmark points on

the critical boundary regions and rerunning the segmentation procedure.

The computational efficiency of the suggested method was not yet thoroughly tested in this study, as the main processing was run with a Matlab code which was not optimized for the speed and memory efficiency. However, excluding the manual setting of the landmark points, the average processing time for a patient data was 390 seconds with a HP EliteBook 8450w laptop (Intel Core i7 CPU, 2.80 GHz, 8GB RAM, 64-bit Windows 7). Normally, the processing efficiency can be improved by more than two orders of magnitude with the C++ code, parallel thread computation and optimized compiler parameters, so we expect to reach computing time less than half minute.

## 6. CONCLUSIONS

We describe a semi-automatic segmentation method for the prostate boundary from the pre-operational MR volume images of the transurethral ultrasonic therapy of the prostate cancer. Two types of MR images were combined in the segmentation method, i.e. the T2-weighted planning image and the T1-weighted preparation image. The results were evaluated with data collected from five patients, and the random landmark positions were simulated to test the robustness. The initial surface model is defined based on the landmarks and anatomical topology, and the final surface deformation is done in the iterative loop by tracking the edges in the direction of the surface normal, which improved the dice similarity coefficient between the reference segmentation. This specific semi-automatic segmentation approach has the benefit of adapting to the MR images having high variation in the quality. Significant changes in the MR scanning protocol might require some re-design of the method, although the constraints set by the anatomical topology are valid for the prostate segmentation in general.

## 7. ACKNOWLEDGMENTS

The study has been supported by the SalWe Research Program for IMO (Tekes - the Finnish Funding Agency for Technology and Innovation, grant 648/10) and the National Institutes of Health (NIH, grant #1R21CA159550).

## 8. REFERENCES

[Ant14a] Antila, K., Nieminen, H. J., Sequeiros, R. B., and Ehnholm, G. Automatic segmentation for detecting uterine fibroid regions treated with MR-guided High Intensity Focused Ultrasound (MR-HIFU), Submitted to Medical Physics as a Technical report, 20 pages, 2014.

[Cho12a] Chopra, R., Colquhoun, A., Burtnyk, M., N'djin, W.A., Kobelevskiy, I., Boyes, A., Siddiqui, K., Foster, H., Sugar, L., Haider, M.A., Bronskill, M., Klotz, L. MR Imaging-controlled Transurethral Ultrasound Therapy for Conformal Treatment of Prostate Tissue: Initial Feasibility in Humans, Radiology 265(1), pp. 303-313, Oct. 2012.

[Dic45a] Dice, L.R. Measures of the amount of ecologic association between species, Ecology, 26(3), pp. 297–302, 1945.

[Kas87a] Kass, M., Witkin, A., and Terzopoulos, D. Snakes: Active Contour Models, Proceedings of First International Conference on Computer Vision, IEEE Comput. Soc. Press, pp. 259-268, 1987.

[Koi04a] Koikkalainen, J., and Lötjönen, J. Reconstruction of 3-D Head Geometry From Digitized Point Sets: An Evaluation Study, IEEE Transactions on Information Technology in Biomedicine, vol. 8 (3), Sep 2004.

[LiQ04a] Li, Q., and Griffiths, J. G. Least Squares Ellipsoid Specific Fitting, Proceedings of the Geometric Modeling and Processing, Beijing, China, April 13- 15, 2004.

[Mic12a] http://promise12.grand-challenge.org/, MICCAI Grand Challenge, Oct 2012.

[Löt99a] Lötjönen, J., Reissman, P.J., Magnin, I., and Katila, T. Model extraction from magnetic resonance volume data using the deformable pyramid, Med. Image Anal., vol. 3, pp. 387–406, Dec 1999.

[Mon11a] Montagnat, J., Delingette, H., and Ayache, N. A review of deformable surfaces: topology, geometry and deformation, Image and Vision Computing 19(14) pp. 1023-1040, 2001.

[NDj12a] N'Djina, W. A., Burtnyk, M., Kobelevskiy, I., Hadjis, S., Bronskill, M. and Chopra, R. Coagulation of human prostate volumes with MRI-controlled transurethral ultrasound therapy: Results in gel phantoms, Med. Phys. 39 (7), pp. 4524-36, July 2012.

[Zou04a] Zou, K. H. Statistical Validation of Image Segmentation Quality Based on a Spatial Overlap Index, Acad Radiol., 11(2), pp. 178–189, Feb 2004.